Chemical Science

Accepted Manuscript

This article can be cited before page numbers have been issued, to do this please use: S. Patra, S. Ghosh, S. Samanta, N. Maurya, S. Das and A. Dey, *Chem. Sci.*, 2026, DOI: 10.1039/D6SC03084J.

ROYAL SOCIETY OF CHEMISTRY

rsc.li/chemical-science

View Article Online
DOI: 10.1039/D6SC03084J

Enhanced and Selective Oxygen Reduction by Iron porphyrin with a Biguanide Residue in the Second Coordination Sphere

Suman Patra †, Soumili Ghosh†, Soumya Samanta, Nisha Maurya, Somnath Das and Abhishek Dey*

School of Chemical Science, Indian Association for the Cultivation of Science, 2A Raja SC Mullick Road, Kolkata, WB, India 700032

Email: icad@iacs.res.in

KEYWORDS : Oxygen reduction, Iron Porphyrin, Pendent biguanide, Micro-solvation, ETPT, PCET

ABSTRACT: The role of 2nd sphere residues in catalytic processes that require multiple-protons and multiple-electrons is a growing area of interest. These 2nd sphere effects manifest through hydrogen bonding, proton transfer and electrostatic interactions resulting in very selective catalysis. Here a biguanide functional group, which can form very strong hydrogen bonding with several water molecules, is installed in the 2nd sphere of an iron porphyrin. The resulting porphyrin, Fe-biguanide, is found to reduce O_2 selectively, by $4e^-/4H^+$, to H_2O in both aqueous, where the biguanide is protonated, and organic medium, where it is neutral, with rates much faster than any porphyrin reported till date. The presence of hydrogen bonding with water molecules in the 2nd sphere is confirmed using several spectroscopic techniques. These results indicate that water molecules, held by 2nd sphere residues, can accelerate the kinetics of $4e^-/4H^+$ reduction of O_2 as well as any other functional group

Introduction

Selective reduction of O_2 by $4e^-/4H^+$ to H_2O is an active area of research which is being pursued by several groups in the world.[1–5] While material-based catalysts can be robust, molecular catalysts offer an opportunity to introduce nuanced changes in the catalyst design to investigate the reaction mechanism in great details resulting in a better understanding of the chemical steps involved in determining the rate and selectivity of O_2 reduction which helps to develop better catalysts for the purpose.[6–9] The $4e^-/4H^+$ reduction of O_2 to H_2O can proceed via large number of combinations of

View Article Online
DOI: 10.1039/D6SC03084J

electron transfer (ET), proton transfer (PT) and proton coupled electron transfer (PCET) steps (**scheme 1**, exemplified using iron porphyrin) which offers several branching points in the reaction landscape which can be controlled through catalyst design. For example, the reduction of a Fe(III)–O_2•$^-$ species, formed after O_2 binding to Fe(II), to a Fe(III)-OOH species can occur either via a PCET or a ETPT or hydrogen atom transfer (HAT) pathways which have all been observed in different synthetic and enzymatic systems and have different demands from their respective transition states.[10–15] Fundamental understanding of the mechanism of O_2 reduction process allows better design of catalysts to navigate through this labyrinth of possible routes.

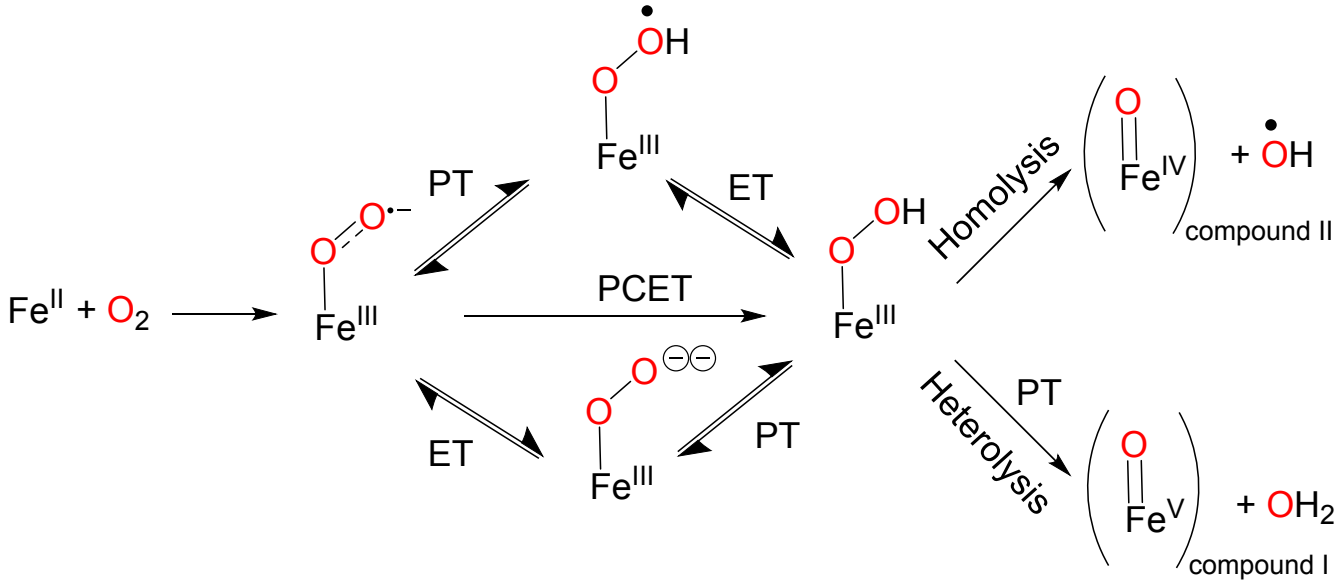

Scheme 1: Mechanistic possibilities of 4e$^-$/4H$^+$ O_2 reduction. Compound I is better described as a Fe(IV)=O unit bound to a porphyrin radical cation.

Iron porphyrins, analogues of the heme active site of cytochrome c oxidase which reduces O_2 to H_2O in mitochondria, have been investigated as potential O_2 reduction catalyst for several decades now. Elaborate models of cytochrome c oxidase have been developed and investigated by several groups. These models have been very useful in understanding the mechanism of O_2 reduction by the metallo-enzyme.[16–20] However, these models require elaborate synthesis and, thus, there has been a constant effort to develop simpler iron porphyrins which can reduce O_2 to H_2O selectively. This will require a detailed understanding of the mechanistic landscape and tools to navigate them.

View Article Online
DOI: 10.1039/D6SC03084J

The O_2 reduction is probed electrochemically both in organic solvents, where the porphyrins are readily soluble, using acids as proton source as well as in aqueous solutions where the porphyrins are adsorbed on graphitic electrodes or on self-assembled monolayers on Au electrodes.[17,21–25] In organic solvents and under homogeneous electrochemical conditions, the rate-determining step of O_2 reduction is the protonation of the Fe(III)–O_2•$^-$ species and in the presence of strong acids it generally results in $4e^-/4H^+$ reduction.[2,26,27] In the case of sterically congested iron porphyrins O_2 binding has been recently reported to be the rds.[28] In-situ spectro-electrochemistry indicates that in the presence of weak acids, the reduction of O_2 proceeds via a ECEC mechanism where the reduction of the iron to its Fe(II) state initiates O_2 binding to result in Fe(III)-O_2^- which is then reduced to a Fe(III)-O_2^{2-} species which is then protonated resulting in the cleavage of the O-O bond.[8,15] In the case of simple porphyrins, a linear free energy-based correlation exists between the rate of O_2 reduction and the overpotential of O_2 reduction, in the presence of strong acids. However, this correlation breaks when 2nd sphere residues that can participate in proton transfer are included in the catalyst.[29,30]

In contrast, in-situ mechanistic investigations of iron porphyrins have revealed that the rate and selectivity of O_2 reduction under heterogeneous conditions in aqueous medium is determined by the fate of a Fe(III)-OOH species. The rate of O-O bond cleavage is the rate determining step and the site of protonation of this species determines the selectivity of O_2 reduction.[31] Protonation of the proximal oxygen of the Fe(III)-OOH species results in the release of H_2O_2, i.e. $2e^-/2H^+$ O_2 reduction, while protonation of the distal oxygen results in O-O bond cleavage and $4e^-/4H^+$ reduction.[7,32,33] However, the mechanism of electrochemical O_2 reduction varies quite a bit depending on the presence of 2nd sphere residues which can hydrogen bond or transfer protons to the active site. Using pendant groups like pyridine, imidazole and amines in the 2nd sphere of iron porphyrins, the rates of O_2 reduction could be enhanced by several orders of magnitude relative to previous reports on elaborate heme/Cu systems while keeping the selectivity for $4e^-/4H^+$ reduction intact. These residues can hydrogen-bond to the Fe(III)-OOH intermediate species, avoiding its hydrolysis which will lead to $2e^-/2H^+$ reduced product H_2O_2, and facilitate proton transfer to the distal oxygen facilitating heterolytic cleavage of the O-O bond.[20–22,34–38]

An unresolved question is the potential role of solvent H_2O molecules in these reactions. While in some cases, the 2nd sphere residue has been proposed to “hold” water molecules, their role/effect in catalysis

View Article Online
DOI: 10.1039/D6SC03084J

has not been unambiguously established.[39] Presence of water cluster near the active site can, in principle, provide the same hydrogen bonding stability to intermediates formed during O_2 reduction and facilitate proton transfer to the active site. However, formation of such clusters near the active site is entropically unfavorable. Investigations on metformin, which is a demethylated biguanide, shows that it strongly hydrogen bonds with the NH terminals of the biguanide group with multiple water molecules in both neutral and protonated forms.[40,41] In this manuscript, an iron porphyrin with a distal biguanide residue is synthesized and its O_2 reduction is investigated in both organic and aqueous medium. The data presented in this manuscript unambiguously demonstrate that indeed, biguanide residues in the 2nd sphere stabilize a cluster of water molecules which in turn facilitate proton transfer to the reaction intermediates resulting in rapid and selective $4e^-/4H^+$ reduction of O_2 to H_2O in both organic and aqueous solvents.

Results

Synthesis

The pendant biguanide group was introduced into the iron porphyrin by reacting (o-aminophenyl) triphenyl porphyrin (H_2MAPP) with cyanoguanidine in the presence of $AlCl_3$, a Lewis acid, in THF solvent under reflux conditions **(Scheme 2)**. The resulting solution was then neutralized with ammonium hydroxide, yielding pure H_2-biguanide after further workup and column chromatography. Hexagoanl purple crystal was obtained by slow evaporation of the ether in DCM (**Fig.1B**). H_2-biguanide was crystallized in C2/c space group. The crystal structure reveals a cluster promoted by intermolecular hydrogen bonding interactions between the polar N–H groups of four H_2-biguanide molecules. These polar biguanide moieties are encapsulated by the planar porphyrin rings, forming a cage-like arrangement (**Fig.1A**). To evaluate the effect of the chelating biguanide moiety on the oxygen reduction reaction, a control porphyrin H_2-triazine was synthesized. This involved blocking the biguanide residue of H_2-biguanide by reacting it with ethyl acetate (**Scheme 1**) in the presence of sodium methoxide as a deprotonating agent, resulting in a 1,3,5-triazine derivative. H_2-triazine was further purified using column chromatography. Both ligands were metalated with $FeBr_2$ salt and collidine as a base in THF solvent under an inert atmosphere, followed by aerobic workup with 4N HCl, resulting in the formation of chloride-bound iron complexes in both cases. Characterization data for the ligands and the iron porphyrins **(Fig. S1-S11& Table-S1)** are provided in the supporting information.

View Article Online
DOI: 10.1039/D6SC03084J

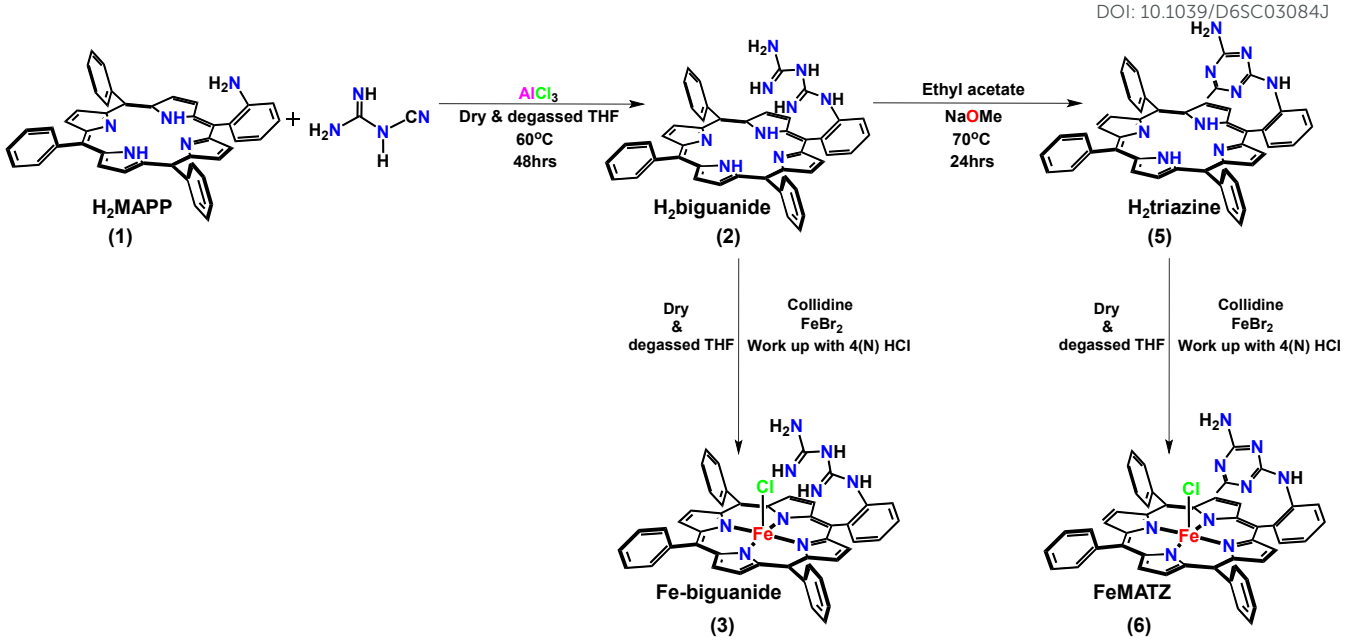

Scheme2. Synthetic procedure adapted to access the complexes investigated.

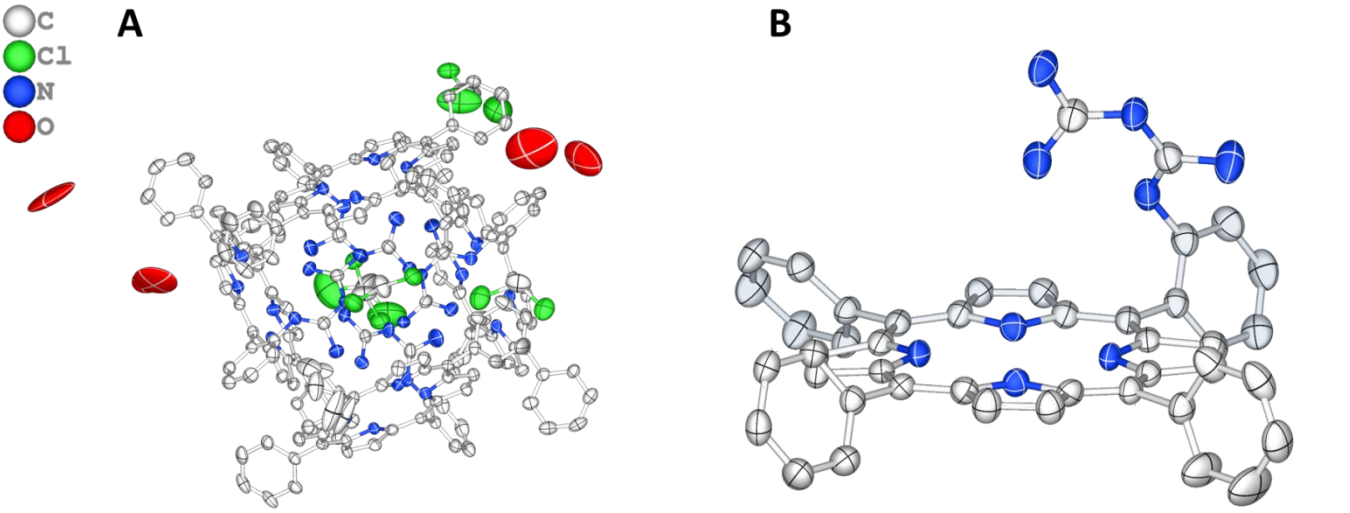

Figure 1. X-ray crystallographic structures of biguanide. Ellipsoid plot of the cluster showing four biguanide macrocycle with coordinated chloride ligands and associated solvent molecules (A). Simplified molecular view highlighting the porphyrin core and the appended biguanide functionality. hydrogen atoms are omitted for clarity (B).

Oxygen Reduction in organic solvents

View Article Online
DOI: 10.1039/D6SC03084J

The electrochemical properties of the Fe–biguanide porphyrin were probed in acetonitrile solvent. Under a nitrogen atmosphere, cyclic voltammetry (CV) revealed a chemically reversible Fe(III/II) redox process at –0.65 V versus Fc^+/Fc^0 (**Fig.2A**, green trace) which is similar to other iron tetraphenylporphyrin derivatives.[20,35] Upon the addition of 5% (v/v) water, this couple shifted anodically by 80 mV, appearing at –0.57 V versus Fc^+/Fc^0 (**Fig.2A**, blue trace). Such an anodic displacement is indicative of microsolvation of the iron site when water is added to the organic solution. This is made possible by the 2nd sphere biguanide residue which can hydrogen bond with several water molecules and thereby form a water cluster in the vicinity of the iron.[39] The presence of microsolvation environment around the iron is further evidenced by the absence of comparable shifts in Fe(III/II) E^0 in the Fe–triazine control complex (**Fig.2B**), in which the biguanide group is blocked and thus incapable of engaging in strong hydrogen-bonding with the added water. This result highlights a secondary coordination sphere effect, whereby the distal functionality, biguanide, tunes redox energetics by as much as 80 mV through microsolvation.

When the Fe–biguanide solution was saturated with O_2, the Fe(III/II) couple became electrochemically irreversible. This behavior is characteristic of oxygen coordination to Fe(II) and subsequent electron transfer to generate a Fe(III)–O_2•$^-$ superoxo intermediate. In the presence of 5% water, a well-defined catalytic wave emerged at –0.80 V versus Fc^+/Fc^0, following a precatalytic feature at –0.7 V **(Fig.2A**, red trace). The separation between the two processes suggests an EC mechanism, in which the electron transfer to Fe–O_2•$^-$ is followed by a chemical step, specifically, protonation of the Fe–O_2^{2-} (peroxide) species. The Fe–triazine did not display any substantial catalytic current under the same conditions in the presence of added water (**Fig.2B**).

View Article Online
DOI: 10.1039/D6SC03084J

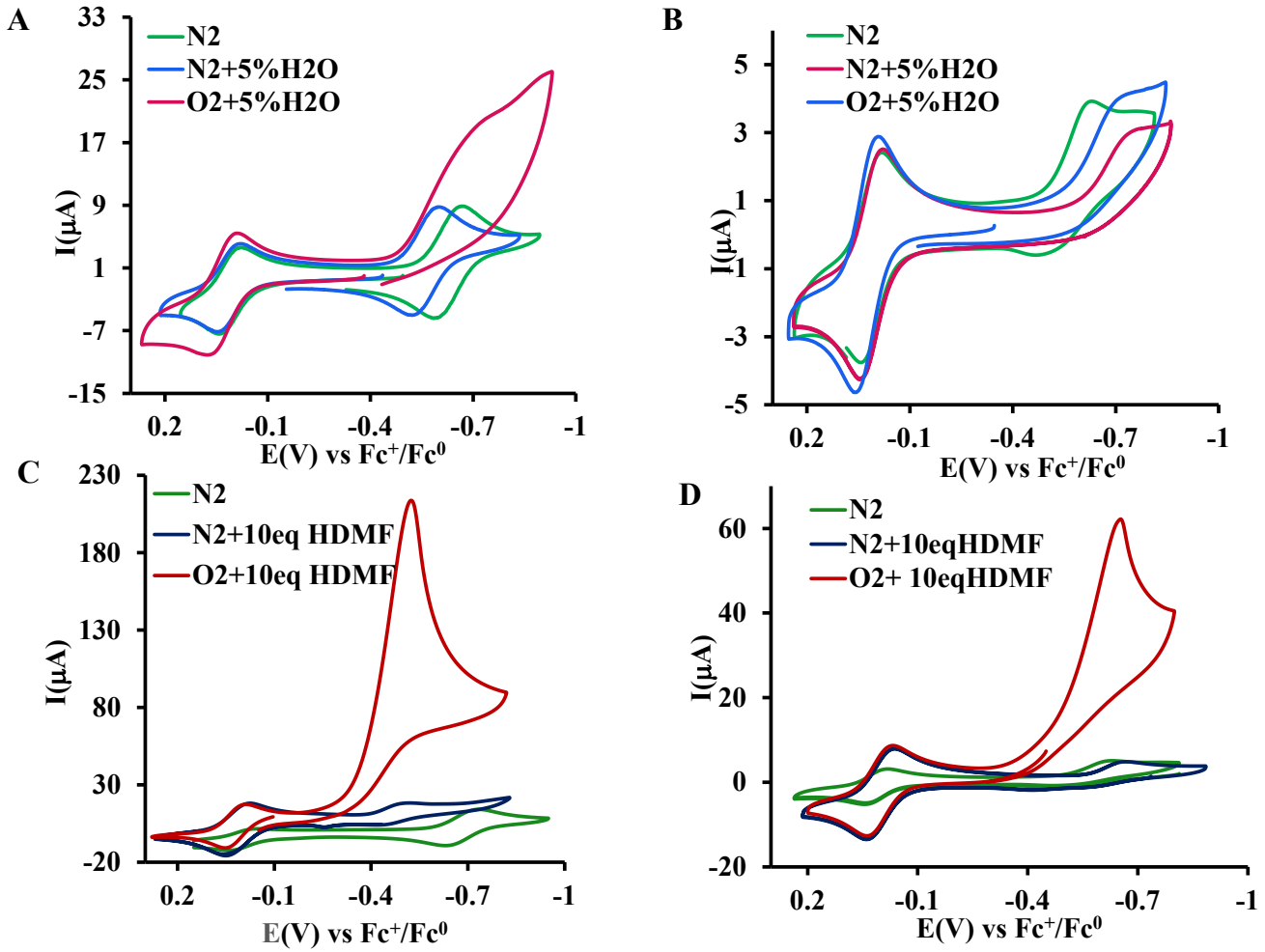

Figure 2. (A) Cyclic voltammograms of Fe-biguanide recorded in CH_3CN under N_2 atmosphere, in the absence and presence of H_2O, and under O_2 atmosphere with added H_2O (B) Identical measurements for Fe-triazine, which serves as the control complex (C) Effect of adding a strong acid (HDMF) to Fe-biguanide solutions, under both N_2 and O_2 atmospheres. (D) Parallel experiments with Fe-triazine in the presence of HDMF.

Iron porphyrins without 2nd sphere assistance typically require strong acids (e.g., trifluoroacetic acid or perchloric acid) to protonate the Fe(III)–O_2•$^-$ intermediate in aprotic media. Water is generally too weak proton source to participate in this step. Previously, Anxolabéhère and co-

View Article Online
DOI: 10.1039/D6SC03084J

workers demonstrated that in the absence of strong acids, the O_2 reduction proceeds through electrochemical conversion of the Fe(III)–O_2•$^-$ to a Fe(III)–O_2^{2-} intermediate, with subsequent protonation by weak acids like $(CF_3)_3C$–OH.[15] Against this backdrop, the observation that a iron porphyrin can catalyze O_2 reduction with water as the sole proton source in an organic solvent is unprecedented. This unique reactivity suggests that the biguanide substituent, which will stay neutral in an organic solvent, not only preorganize water molecules around the porphyrin periphery but may also effectively tune the pK_a of the reactants involved, thereby rendering proton transfer to the bound oxygen intermediates through extended hydrogen-bonding network. Such organization of water molecules could potentially stabilize protonated water clusters or "caged hydronium" motifs resembling Zundel- or Stoyanov-like structures[42] which is consistent with the observed reactivity trends. Density Functional Theory (DFT) was used to examine the spatial arrangement of the appended biguanide group relative to the iron center and the axial ligand environment. The optimized structure supports the proposed secondary coordination sphere interaction, showing intramolecular hydrogen bonding between the axial Fe–OH ligand and the appended biguanide –NH group, with an H–O···H–N distance of 1.79 Å. These results support the feasibility of the proposed hydrogen-bonding interaction **(Fig. S12).** However accurate modelling in the presence of explicit water clusters and hydrogen-bonding network would require extensive computational treatment which is beyond the scope of the present work**.**

The catalytic performance of Fe–biguanide and Fe-triazine were benchmarked in the presence of HDMF (protonated DMF) as the proton donor (**Fig. 2C, 2D**). Under acidic conditions the Fe(III/II) redox process, probed under N_2 atmosphere, shifts to -0.49 V vs Fc/Fc^+ which is 160 mV anodically shifted with respect to its value in the absence of acid. This is likely the result of protonation of the biguanide residue in the 2nd sphere which results in a positively charged electrostatic potential near the iron. In the presence of HDMF, a O_2 reduction current is observed which peaks at Fe(III/II) potential (**Fig.2C**). Under acidic conditions, oxygen reduction follows a CE pathway in an organic solvent, in which the Fe(III)–O_2•$^-$ superoxide intermediate undergoes protonation prior to electron transfer such that the protonation is the rate determining step and all subsequent steps are relatively rapid.[11] As a result the Fe(III)–O_2•$^-$ superoxide species is the only intermediate observed under these conditions. The anodic shift of the Fe(III/II) reduction potential in the presence of acid, thus, automatically lowers the overpotential of O_2 reduction. The kinetic parameters, including

View Article Online
DOI: 10.1039/D6SC03084J

kobs, TOFmax, and onset values obtained by foot-of-the-wave analysis (FOWA), are summarized in **Table 1** (**Fig. S13**).

The rate of ORR catalyzed by Fe-biguanide under these conditions is 8510 $M^{-1}s^{-1}$. The rate of FeTPP, which does not have any 2nd sphere residues, under the same condition is 309 $M^{-1}s^{-1}$. The rate of Fe-triazine is 600 $M^{-1}s^{-1}$ which is similar to FeTPP. The data clearly establish Fe–biguanide as the superior catalyst, having both lower overpotential and significantly higher catalytic turnover relative to FeTPP and Fe–triazine. Importantly, Fe–biguanide reaches TOF values nearly 14-fold greater than Fe–triazine at a lower overpotential, illustrating how the second-sphere biguanide residue favorably affect both the kinetics and thermodynamics of ORR (**Table1**). In fact, the Fe-biguanide surpasses the kinetic rates of similar iron porphyrins with pyridine (FeL2, **Table 1**), dibenzylamine (FeDB, **Table 1**) and imidazole (FeMIm, **Table 1**). Needless to say, the higher O_2 reduction rate at lower overpotential contradicts the expected trend based on scaling relationship forwarded in the past.[30] This is a characteristic of iron porphyrins with proton transfer residues in the 2nd sphere.[35]

EPR measurements of Fe(III)-biguanide showed a characteristic high-spin Fe(III) signal at (g = 6), indicating the absence of μ-oxo dimer formation, as μ-oxo Fe(III) porphyrins are typically EPR silent due to antiferromagnetic coupling (**Fig S14A**). Additionally, controlled potential electrolysis (CPE) under O_2-saturated conditions showed less than 10% catalyst degradation after 1 h. Both pre- and post-electrolysis UV–vis spectra displayed a Soret band at 416 nm, characteristic of monomeric Fe(III) porphyrins, whereas μ-oxo species typically exhibit a Soret band around 410 nm. The high ORR catalytic rate of Fe-biguanide (8510 $M^{-1}s^{-1}$) further supports the absence of μ-oxo formation under electrochemical conditions (**Fig S14B,C**).

Table 1. Comparative catalytic parameters for oxygen reduction by FeTPP, Fe–biguanide, Fe–triazine, Fe-DB, Fe-OB, FeL2, Fe-TPPMIm in CH_3CN with HDMF and TsOH as the proton source.

2nd Sphere	**k_obs (10^2 $M^{-1}s^{-1}$)**	**TOF_max (s^{-1})**	**Overpotential (V)**	**Proton source**	**Reference**
No 2nd sphere (FeTPP)	3.09	2.50	1.38	HDMF	This work

View Article Online
DOI: 10.1039/D6SC03084J

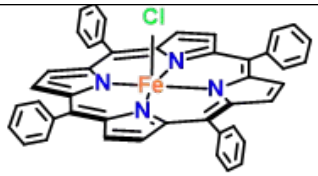					
Biguanide (Fe–biguanide) 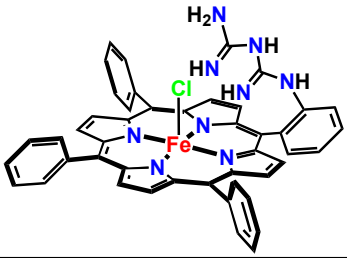	85.1	68.1	1.14	HDMF	This work
Triazine (Fe–triazine) 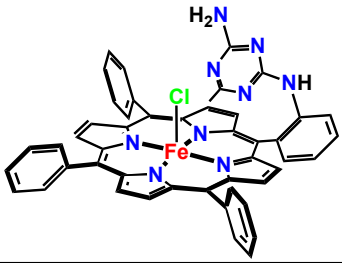	6.00	4.80	1.27	HDMF	This work
2-dibenzyl amine (Fe-DB) 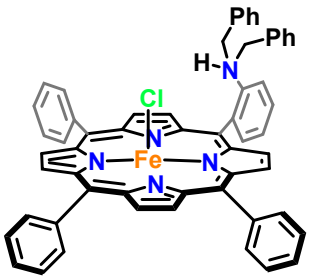	12.8	10.3	1.08	TsOH	35
4-dibenzyl amine(FeOB) 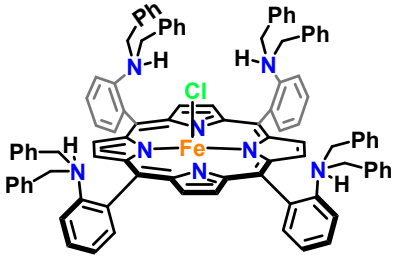	15.4	12.3	1.01	TsOH	35

View Article Online
DOI: 10.1039/D6SC03084J

Pyridine (FeL2) 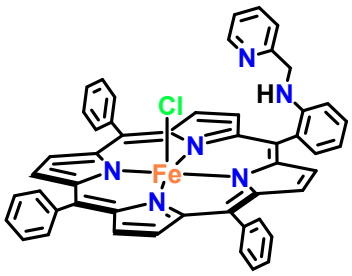	7.8	6.25	1.05	TsOH	35
No second sphere (FeTPP) 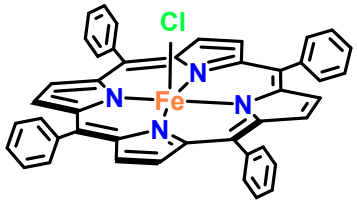	1.99	1.59	1.20	TsOH	35
Imidazole (FeTPPMIm) 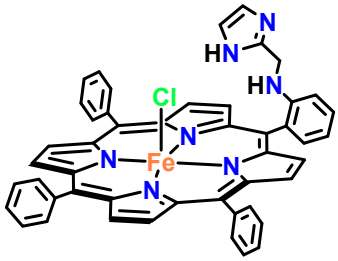	16	13	1.10	TSOH	20

Microsolvation environment of Fe-biguanide

A key question that arises from the reactivity exhibited by Fe–biguanide is how O_2 reduction in organic solvents can proceed at all using a weak acid source like water, when all other iron porphyrins need stronger acid sources. Several complementary spectroscopic studies were employed to probe the interaction of the biguanide group in the 2nd sphere with water in the medium. ^{1}H NMR spectroscopy of the free H_2-biguanide-porphyrin ligand in DMSO-d_6 show that the ^{1}H resonance of the dissolved water (750mM, chosen arbitrarily) is at 3.392 ppm whereas it is found at 3.355 ppm in DMSO d^6-. The water content in DMSO-d_6 was quantified using the –OMe

View Article Online
DOI: 10.1039/D6SC03084J

(9H's) resonance of 10 mM 1,3,5-trimethoxy-benzene as an internal standard (**Fig. 3**). The observed downfield shift of the water signal in the presence of H_2-biguanide supports hydrogen bonding interactions, which weaken the O–H bond. Upon increasing the water content from 2 M to 15 M in both neat DMSO-d_6 and DMSO-d_6 containing H_2-biguanide, the water resonance shifts progressively downfield (**Fig. S15-S18**). The shift in DMSO-d_6 arises from enhanced water–water as well as water–DMSO hydrogen-bonding interactions. However, in the presence of H_2-biguanide, the water signal is always shifted ~0.1 ppm further downfield compared to neat DMSO-d_6, indicating additional interaction between water and the biguanide moiety. To confirm, whether this interaction originate from the biguanide unit itself, the experiment was repeated using phenyl-biguanide (lacking the porphyrin core), which produced a comparable downfield shift of the water resonance to that observed with H_2-biguanide (**Fig. S15-S18**).

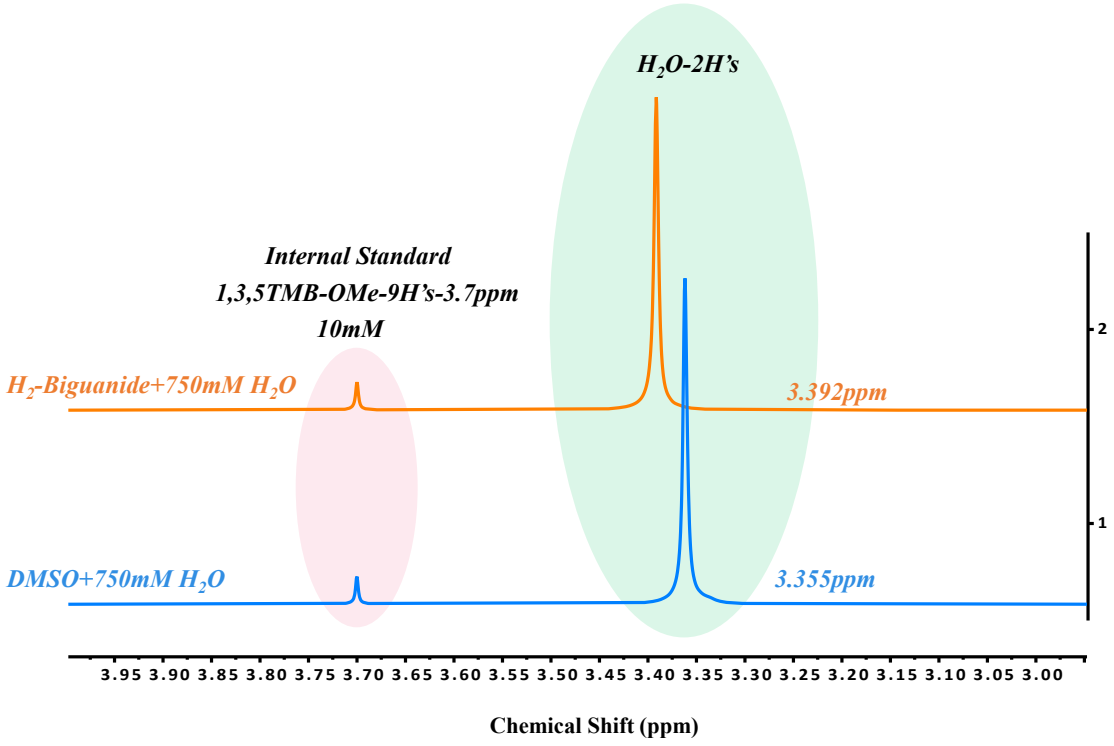

View Article Online
DOI: 10.1039/D6SC03084J

Figure 3. ^{1}H NMR spectra of DMSO-d_6 + 750mM (blue spectra), and H_2-biguanide+750mM H_2O (orange spectra).

The presence of water in the vicinity of the porphyrin can be evidenced more directly by using TCSPC (Time Correlated Single Photon Counting). Local water molecule quenches the excited state rapidly leading to shorter excited state lifetimes. Fluorescence studies of Zn–biguanide (a fluoroscent analogue of Fe-biguanide) revealed that emission properties are highly sensitive to the presence of water in the medium. In dry DMSO, Zn–biguanide displayed a sharp emission peak at 452 nm with a lifetime of 3.21 ns (**Fig.4A**) whereas no emission peak at 452nm was observed for Zn-triazine (**Fig.4B**) . Incremental water addition progressively quenched the emission, and at 5% water the lifetime decreased to 1.54 ns, representing nearly a 50% reduction (**Fig.4C**) of the excited state lifetime. No such effect was observed in Zn–triazine, confirming that the biguanidinium groups are directly responsible (**Fig.4D**) for hoarding water molecules in the vicinity of the active site as has been indicated by the ^{1}H NMR in DMSO-d_6. A satisfactory fit was confirmed when the weighted residuals were randomly distributed around zero. **(Fig. S19)**

View Article Online
DOI: 10.1039/D6SC03084J

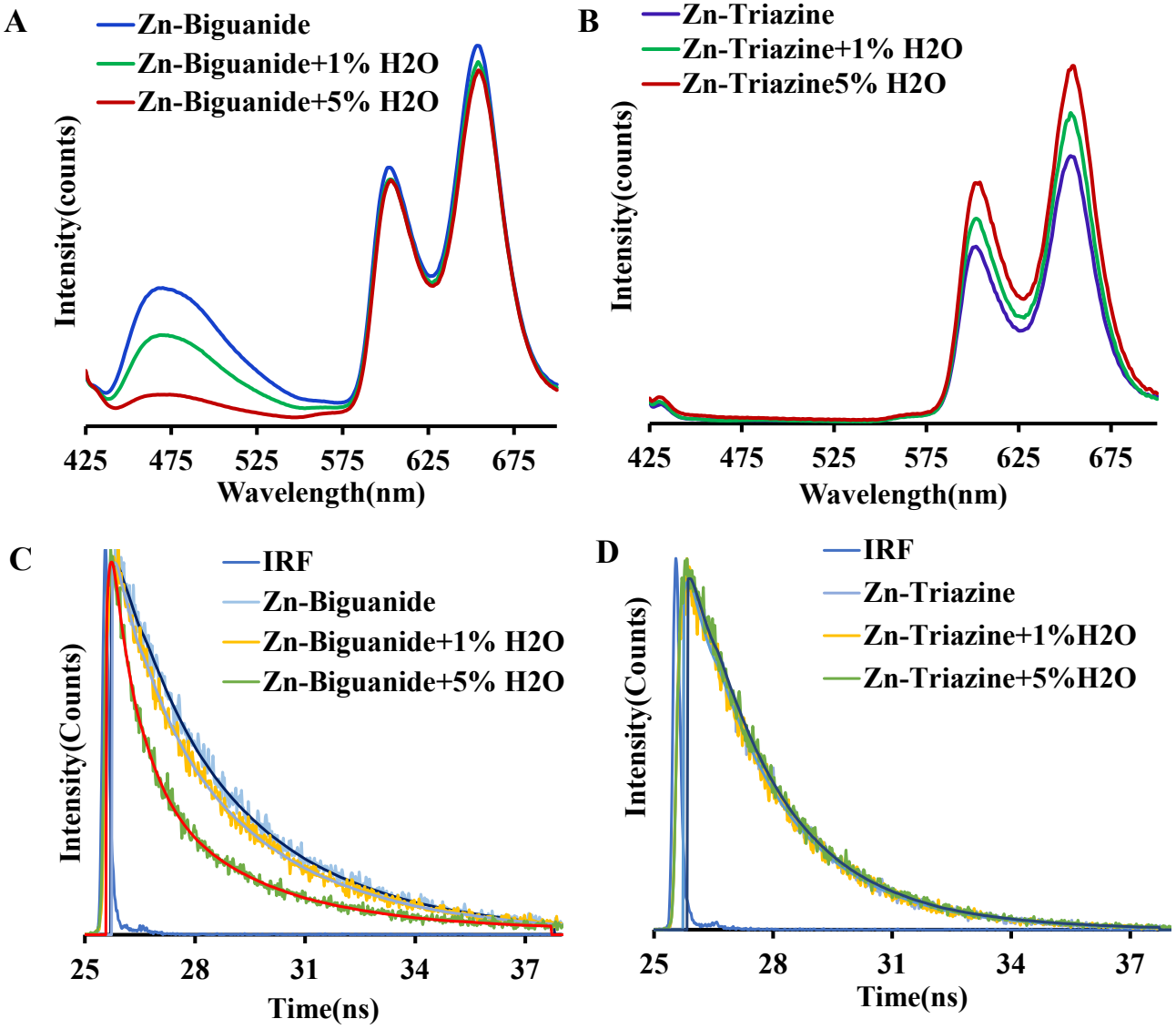

Figure 4. (A) Emission spectra of Zn–biguanide in pure acetonitrile and in the presence of 1% and 5% H_2O, showing progressive quenching of fluorescence intensity with increasing water fraction. (B) Corresponding spectra for Zn–triazine under identical conditions, displaying only minimal changes in intensity upon water addition. (C) Time-resolved fluorescence decay profiles of Zn–biguanide with increasing water content, demonstrating a marked decrease in excited-state lifetime as the H_2O percentage increases, consistent with enhanced non-radiative deactivation. Instrument response function (IRF) represents the temporal response of the detection system to an instantaneous excitation pulse and is used for accurate fluorescence lifetime analysis. (D) Decay profiles for Zn–triazine in acetonitrile with 1% and 5% H_2O, showing only slight modulation of lifetime relative to Zn– biguanide.

View Article Online
DOI: 10.1039/D6SC03084J

Heterogeneous O_2 Reduction Reaction

The Fe–biguanide complex was immobilized on edge-plane graphite (EPG) electrodes and on self-assembled monolayer (SAM)-modified Au electrodes via drop-casting, and their electrochemical responses were recorded in pH 7 phosphate buffer solutions. At this pH, the biguanide residue should be protonated as the pK_a of phenylbiguanide is ~11.0.[40,43] In the absence of O_2, the complex exhibited an electrochemically reversible Fe(III/II) redox couple, with half-wave potentials ($E_1/_2$) of –320 mV vs Ag/AgCl on octanethiol (C_8SH) SAM and –328 mV on EPG (**Fig.5A**). Upon exposure to O_2, the reversible Fe(III/II) feature is replaced by a diffusion-limited catalytic wave corresponding to O_2 reduction, with peak potential similar to the Fe(III/II) $E_{1/2}$ on EPG (**Fig. 5A**) as well as on C_8SH-SAM (**Fig.S20**). Rotating disk electrode (RDE) measurements revealed that the catalytic current increased proportionally with rotation rate, indicating mass transport-controlled kinetics (**Fig.5B**). Koutecky–Levich (K–L) analysis yielded a linear relationship between $1/I_{cat}$ and $1/\omega^{1/2}$, with a slope consistent with a four-electron reduction of O_2 to water (**Fig.5C**). From the K–L intercept, the second-order rate constant (k_{cat}) was determined to be 2.5×10^7 M^{-1} s^{-1}, approximately an order of magnitude higher than the Fe–porphyrin bearing triazine (**Fig.S21**) or guanidine substituents, implying that the definite role of the biguanide 2nd sphere functionality in facilitating O_2 reduction extends to aqueous medium as well (**Table 2**).

View Article Online
DOI: 10.1039/D6SC03084J

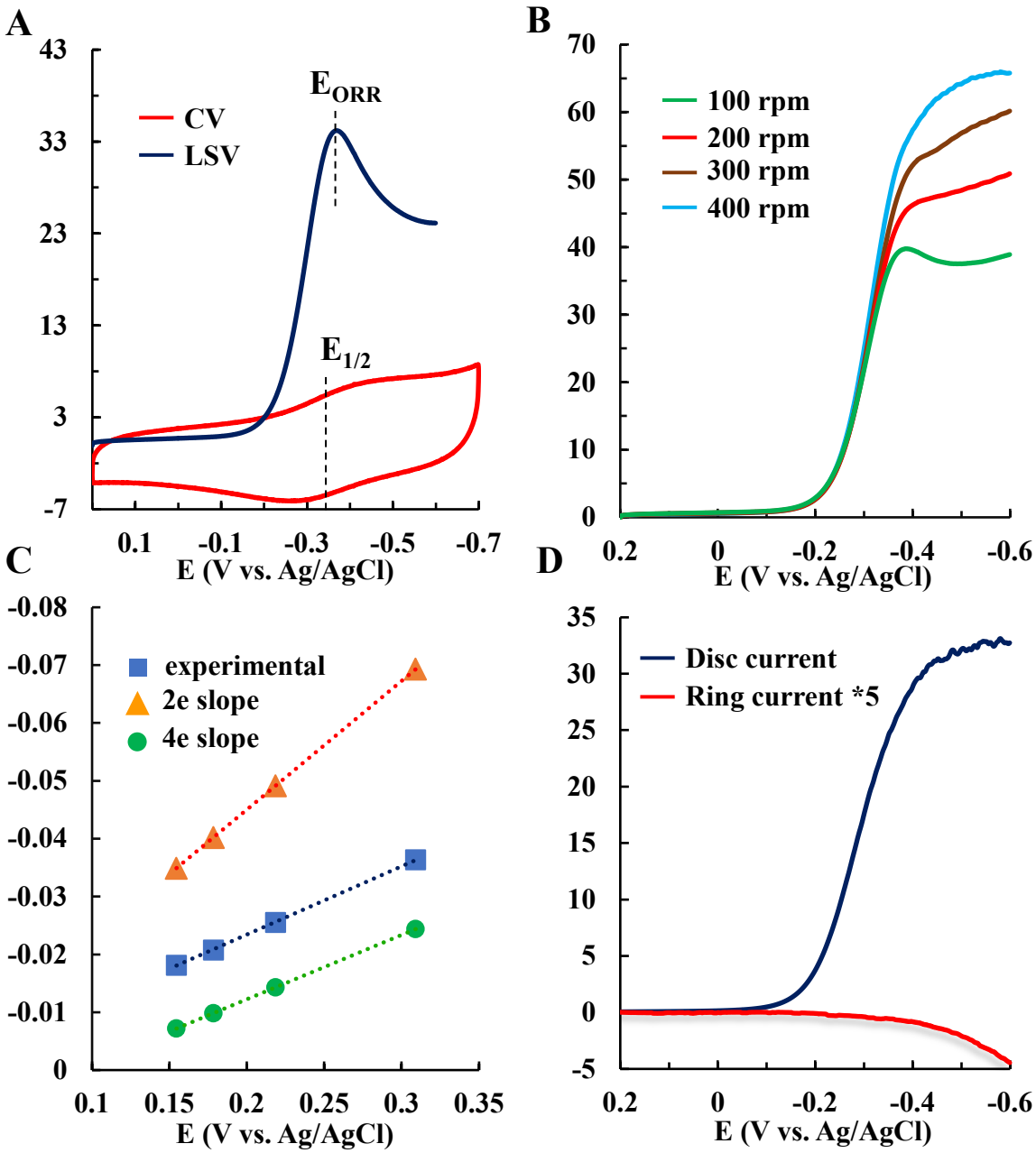

View Article Online
DOI: 10.1039/D6SC03084J

Fig5. (A) Cyclic voltammograms of Fe–biguanide recorded under N_2 and O_2 atmospheres in pH 7 phosphate buffer on EPG, showing the reversible Fe(III/II) couple under N_2 and the appearance of a catalytic wave in O_2. (B) Linear sweep voltammograms at a rotating disk electrode (RDE) at various rotation rates, displaying diffusion-limited catalytic currents consistent with multi-electron oxygen reduction. (C) Koutecký–Levich (K–L) analysis of the RDE data at different potentials, yielding linear fits that confirm first-order dependence on O_2 concentration and establish the number of electrons transferred per O_2 molecule, consistent with a $4e^-/4H^+$ pathway to H_2O. (D) Rotating ring–disk electrode (RRDE) experiment showing the disk current corresponding to O_2 reduction and the simultaneous ring current for peroxide detection, indicating high selectivity for complete $4e^-$ reduction with only minor H_2O_2 release.

Selectivity for $4e^-$ Reduction and PROS Analysis

O_2 reduction can proceed via either a $2e^-/2H^+$ pathway producing H_2O_2 or a $4e^-/4H^+$ pathway producing H_2O. The RDE data indicate that the O_2 reduction involves the delivery of $4e^-$ (**Fig.5C**, n=4). Selectivity was further evaluated using rotating ring-disk electrode (RRDE) experiments, which detect partially reduced oxygen species (PROS) released from the working electrode and oxidized at the surrounding Pt ring (**Fig. 5D**).[44] PROS during O_2 reduction in aqueous medium results from the hydrolysis of the Fe(III)-OOH intermediate.[45] On EPG, Fe–biguanide generated only ~6% PROS, corresponding to 94% selectivity for complete $4e^-/4H^+$ reduction (**Table 2**) consistent with the RDE data. The negligible release of H_2O_2 indicates stabilization of the Fe(III)-OOH species against hydrolysis by the 2nd sphere biguanide residue by hydrogen bonding. This stability is tested better under slow electron transfer (ET) rates. Au electrodes functionalized with SAMs of varying alkyl chain lengths (C_8SH and hexadecanethiol $C_{16}SH$) were employed. As the chain length increases, electron tunneling slows down substantially, providing more time for partially reduced species to diffuse before full reduction (~10^3 s^{-1} in C_8SH ~4–6 s^{-1} $C_{16}SH$ and > 10^5 s^{-1} in EPG). [46–49] Even under these slow ET conditions, PROS formation increased only modestly to 9.0 % on C_8SH-SAM and 11.7% on $C_{16}SH$-SAM (**Table 2**), indicating that Fe–biguanide maintains high selectivity for complete O_2 reduction across a broad range of ET rates.

View Article Online
DOI: 10.1039/D6SC03084J

Table2. Kinetics and selectivity of oxygen reduction by Fe–biguanide under heterogeneous conditions.

Catalyst		Kinetics of ORR	PROS analysis		
Fe-biguanide		k_{cat} ($1*10^6$) (M^{-1} s^{-1})	EPG	C_8SH-SAM	C_{16}SH-SAM
	H_2O	25.02± 0.32	5.6	9.0	11.7
	D_2O	8.30± 0.22	2.4	3.0	4.6
	H/D	3.0	2.3	3.0	2.5

Kinetic Isotope Effect

The rate of O_2 reduction on EPG electrode decreased to 8.3×10^6 M^{-1} s^{-1} in D_2O, yielding a kinetic isotope effect (KIE) of ~3.0 (**Table 2**). This indicates that a proton transfer or a proton-coupled electron transfer (PCET) is involved in the rate-determining step (rds).[27] Additionally, the KIE on PROS indicates that the step responsible for the generation of PROS involves protonation or PCET. Past mechanistic investigations on iron porphyrins using surface enhanced resonance Raman coupled to rotating disc electrochemistry have indicated that PROS is generated via the protonation of a Fe(III)-OOH intermediate species (pK_a ~7) generated during O_2 reduction to release H_2O_2.[45] Thus, the KIE in PROS generation is consistent with the protonation of the Fe(III)-OOH to release H_2O_2. The KIE on the rate of ORR recorded on a thiolate bound iron porphyrin without a distal super structure was 18 owing to the lack of proton transfer pathways to the catalytic active site.[27] The low KIE of 3.0 in Fe-biguanide is consistent with a well-organized proton transfer channel during ORR.

Identification of Catalytic Intermediates

SERRS-RDE technique was developed to identify the reactive intermediates formed during catalytic ORR activity on heterogeneous electrodes using a home built set-up combining in-situ surface enhanced resonance Raman spectroscopy and rotating disc electrochemistry.[50,51] Oxygen reduction is a multistep process involving delivery of $4e^-$ and $4H^+$ to O_2 during the catalytic cycle. Under steady state conditions, different oxygen bound intermediate species gets accumulated depending on the rds of the ORR cycle i.e. the intermediate with the slowest decay rate accumulates under steady

View Article Online
DOI: 10.1039/D6SC03084J

state. If these intermediates can be identified, direct characterization of the key intermediate species that dominates the rate and selectivity of the overall process can be attempted. When excited into Soret region, iron porphyrin complexes exhibits intense Raman bands characteristic of the metal ligand as well as oxidation and spin states.[52–54] In particular, the v_4 and the v_2 marker bands represent the oxidation state, spin state and coordination number of the iron with high fidelity. The Fe-biguanide complex immobilized over C_8SH modified Ag electrode shows presence of Fe^{III} HS only marked by v_4 and v_2 at 1365 cm^{-1} and 1555 cm^{-1}, respectively **(Fig. 6B**), when the electrode is held at 0V in pH7 buffer indicating a high spin Fe(III) resting state of the iron porphyrin. In the low energy region of the SERRS data a band at 582 cm^{-1} is observed (**Fig.7A**) , which loses intensity upon reduction of Fe^{II}, which arise from Fe-O stretch of hydroxide ligand to the Fe^{III}-biguanide complex under aqueous solutions.[55]

View Article Online
DOI: 10.1039/D6SC03084J

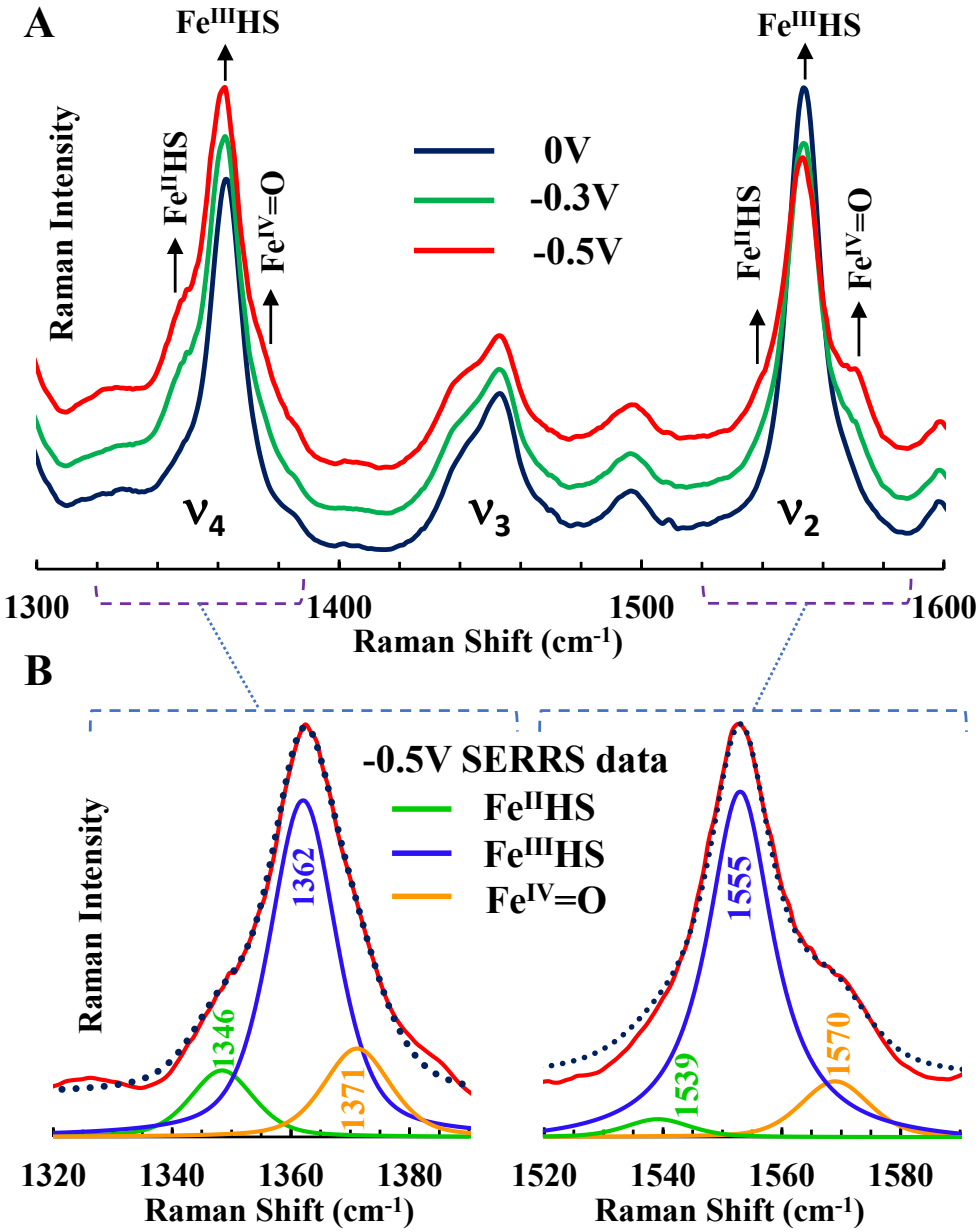

Figure 6. (A) Surface-enhanced resonance Raman spectra (SERRS) of Fe–biguanide immobilized on C8SH–modified Ag electrode recorded under air-saturated pH 7 buffer at different applied potentials (top). (B) Deconvolution of the ν_4 (left) and ν_2 (right) regions reveals the coexistence of Fe(III) HS and Fe(II) HS states, along with the emergence of new bands at 1371 cm^{-1} and 1570 cm^{-1}, assigned to ferryl (Fe(IV)=O) species accumulated under catalytic turnover. (below)

View Article Online
DOI: 10.1039/D6SC03084J

In the absence of O_2, applying potential below the $Fe^{III/II}$ $E_{1/2}$ results conversion of the resting high spin Fe(III) to high spin Fe^{II} indicated by downshift of the ν_4 and ν_2 to 1344 cm^{-1} and 1543 cm^{-1}, respectively (**Fig.S22**). Under catalytic conditions in air saturated buffer, this Fe^{II} HS marker bands is replaced by broad bands indicating presence of mixture of species (**Fig. 6A**). The deconvolution of the ν_4 and ν_2 peaks shows rise of ν_4 and ν_2 bands at 1371 cm^{-1} and 1570 cm^{-1}, respectively, along with residual Fe^{III} HS and Fe^{II} HS species with ν_4 and ν_2 vibrations at 1362, 1555 and 1346, 1539, respectively. These high energy marker bands(1371, 1570) indicate the accumulation of ferryl (Fe^{IV}=O) species during ORR.[21,56] As the potential was lowered from -0.3V to -0.5V, these 1370 cm^{-1} and 1571 cm^{-1} bands gradually gains intensity indicating that this species is indeed formed during the course of ORR.

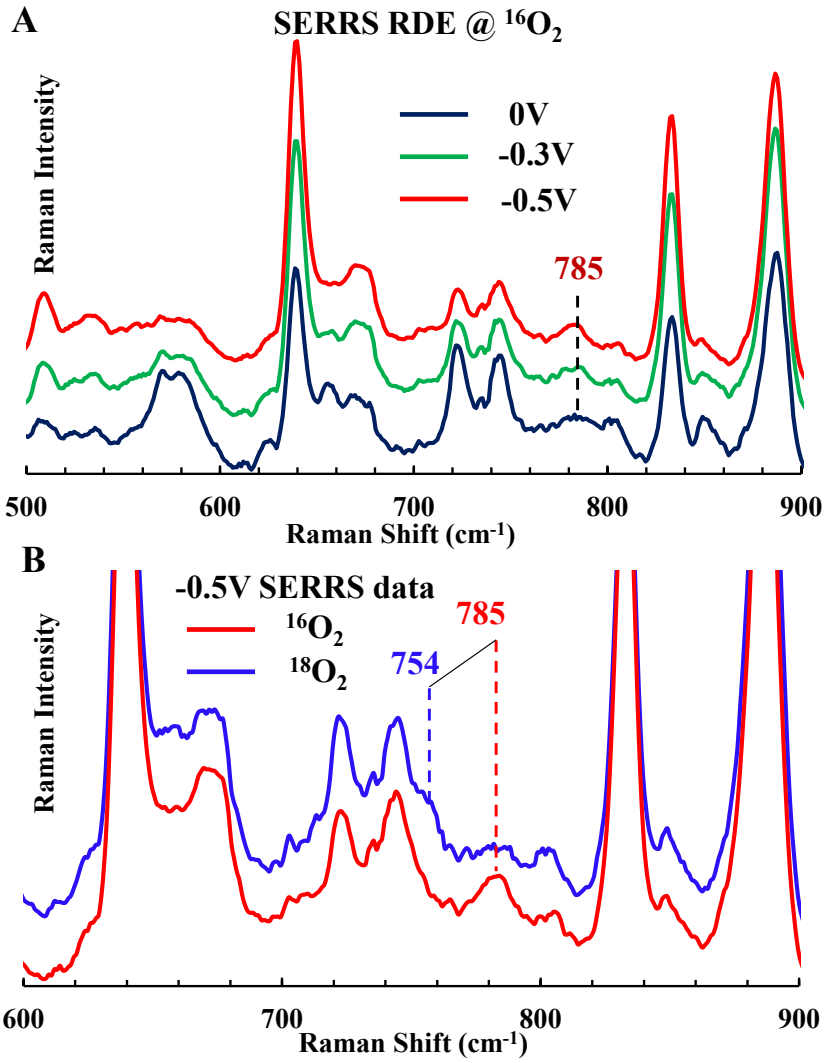

View Article Online
DOI: 10.1039/D6SC03084J

Fig7. (A) Low-frequency region of the SERRS-RDE spectra showing the formation of the Fe(IV)=O species, evidenced by a band at 785 cm^{-1} upon applying potentials from 0 to –0.5 V. (B) The band shifts to 754 cm^{-1} when $^{18}O_2$ is used instead of $^{16}O_2$, confirming the isotopic substitution of the oxo species.

Examining the lower energy region of the SERRS data helps identify metal-oxygen stretching frequencies that can be confirmed using labeled $^{18}O_2$. In air saturated pH7 buffer, a new band rises in intensity 785 cm^{-1} as the potential of the working electrode is lowered (**Fig. 7A**). When the buffer is saturated with $^{18}O_2$, this bands shifts to 754 cm^{-1} **(Fig. 7B)**. The observed isotopic shift of 31 cm^{-1} with ^{18}O substitution is in good agreement with the calculated value for a diatomic Fe–O oscillator for a Fe^{IV}=O species confirming its accumulation on the electrode during catalytic O_2 reduction. This implies that reduction of the Fe^{IV}=O is the rds in catalytic O_2 reduction. Note that the accumulation of the Fe^{IV}=O species during catalysis indicates that the reduction of Fe^{IV}=O to Fe^{III}-OH is a PCET process which is consistent with the KIE observed.

The rate of ORR and its selectivity for $4e^-/4H^+$ of Fe-biguanide is highest among all iron porphyrin complexes reported in pH 7 buffered solution. These porphyrins differ in their rds and its difficult to compare rates of iron porphyrins having different rds (**Table 3**). The only clear comparison can be with Fe-MARG which has a guanidine group instead of a biguanide group in Fe-biguanide. Both of these show the accumulation of Fe(IV)=O species during catalytic steady state as indicated by the SERRS-RDE data. The guanidine group should also be protonated at pH 7 and, in that way, is similar to biguanide. However, the guanidine groups will not be able to hold on to as many water molecules in its distal cavity as biguanide as the later has more tethering points for hydrogen bonding with water molecules.[57] In organic solvents, Fe-MARG does not show ORR in the presence of H_2O in the solvent unlike Fe-biguanide (**Fig. S23**). This again reflects the inability of guanidine to stabilize H_2O molecules in the 2nd sphere. This is the reason for more facile ORR in Fe-biguanide relative to Fe-MARG in organic as well as aqueous medium.

View Article Online
DOI: 10.1039/D6SC03084J

Table 3: The ORR kinetics and selectivity of the Fe-biguanide and some related iron porphyrins in pH 7 buffered solution. An extensive list is included in (**Table S2**).

2nd sphere	K_{ORR} (x10^6) $M^{-1}s^{-1}$	PROS	KIE	Rds species	Reference
Biguanide (Fe-Biguanide) 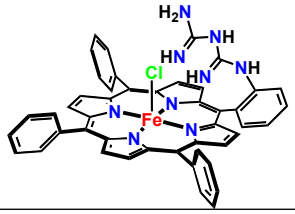	25.02± 0.32	5.6	3	Fe(IV)=O	This work
Pyridine (FeL2) 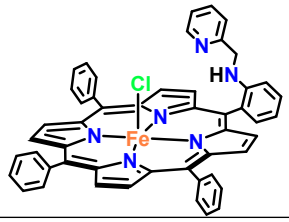	18.0	5	-	Fe(III)-OOH	34
Imidazole (Fe-TPPMIm) 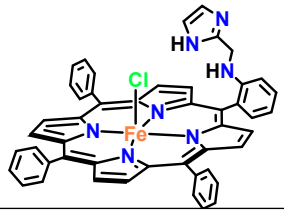	8.34	2.2	-	Fe(III)-OOH	20
4 dibenzylamine (Fe-OB) 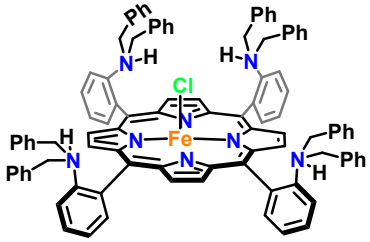	22.0	6.1±0.3	10.6	Fe(III)-$O_2^{\cdot-}$	35
2 dibenzylamine (Fe-DB)	7.26±0.3	2.3±0.2	1.9	Fe(III)-OOH	35

View Article Online
DOI: 10.1039/D6SC03084J

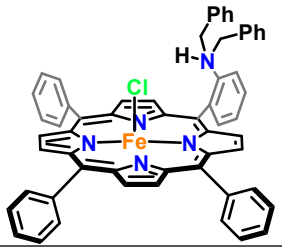					

Conclusion

The Fe–biguanide porphyrin represents a rare and mechanistically distinct case where water molecules can mediate the oxygen reduction reaction in a non-aqueous solvent. The key enabling factor is the distal biguanide group, which holds water molecules in the 2nd sphere, modulates the redox potential through microsolvation and enables catalytic O_2 reduction at relatively low overpotentials, with TOFs exceeding those of conventional iron porphyrins by more than an order of magnitude and low H/D KIE. This work further underscores the prowess of secondary-sphere effects in molecular electrocatalysis, where substituents can create local solvation environments that fundamentally alter proton availability and catalytic pathways. The results point toward broader opportunities in catalyst design where weak acids, such as water in organic solvents, can be rendered chemically competent through tailored second-sphere interactions as demonstrated here.

Experimental Section

Materials: All reagents were of the highest grade commercially available. Dicyanodiamide and $AlCl_3$ was purchased from Sisco Research Laboratories (SRL). 2,4,6-collidine, $FeBr_2$, $Zn(OAc)_2$, chloroform-d_3, tetrabutylammonium perchlorate (TBAP) and ferrocene (Fc) were purchased from Sigma-Aldrich. Sodium chloride and ammonium chloride were purchased from Spectrochem Ltd. Unless otherwise mentioned, all reactions were performed at room temperature. Column chromatography was performed with silica gel (mesh size: 100–200) preparative-scale TLC,

View Article Online
DOI: 10.1039/D6SC03084J

performed with silica gel GF-254 (~13% $CaSO_4$, 0.5H $_2$O binders with a fluorescent indicator) was purchased from Spectrochem Ltd. Neutral alumina was purchased from Merck. Tetrahydrofuran (THF), ethylacetate and acetonitrile (CH_3CN) were purchased from FINAR, Ltd. THF was used after drying over Na metal with the addition of benzophenone indicator and CH_3CN was dried over $CaCl_2$ and CaH_2.

Instrumental details: All electrochemical experiments were performed using CH instruments (CH 700E electrochemical analyser). Glassy carbon, platinum, and standard double-junction Ag/AgCl

reference electrode (standard double-junction silver/silver chloride filled with4 M KNO_3 solution) were purchased from Pine Instruments. All the NMR spectra were recorded on a Bruker DPX-300, Bruker DPX-400, or DPX-500 spectrometer at room temperature. The mass spectra were recorded by the QTOF Micro YA263 instrument. Steady state absorption spectra were measured using an Evolution 201 (ThermoFisher) UV−vis spectrophotometer. The slit width was kept at 2 nm and the experiments are carried out in room temperature. Fluorescence measurements were carried out using Fluoromax 4 (HORIBA Scientific) in room temperature. The slit width was fixed at 2 nm. The lifetime of complexes in different conditions was estimated by measuring the emission decays of the samples using the Time-Correlated Single Photon Counting (TCSPC) setup of Deltaflex (HORIBA). The laser source of 405 nm with full width at half-maximum (FWHM) of 900 ps was used for the TCSPC experiments. The emission decays were collected at the magic angle polarization and detected using a photomultiplier tube. EzTime software was used to fit the decay traces. All electrochemical experiments were conducted using CH Instruments (model CHI700E, CHI720D Electrochemical Analyzer). The bipotentiostat, reference electrodes, and Teflon plate material evaluating cell (ALS Japan) were purchased from CH Instruments. The RRDE setup from Pine Research Instrumentation (E6 series Change Disk tips with AFE6M rotor) was used to obtain RRDE data. SERRS-RDE data were collected using a Trivista 555 spectrograph (Princeton Instruments) and 413.1 nm excitation from a Kr+ laser (Coherent Innova Saber SBRCDBW-K), rotating the electrode at 200 rpm unless noted otherwise. The region of interest in the Raman spectrum was calibrated against naphthalene resonance Raman spectra during each instance of data collection. X-ray single-crystal data were collected on a Bruker D8VENTURE Microfocus diffractometer equipped with PHOTON II Detector, with Mo Kα radiation (λ = 0.710 73 Å), controlled by the APEX3 software package. 87 Raw data were integrated and corrected for Lorentz and polarization effects using the

View Article Online
DOI: 10.1039/D6SC03084J

Bruker APEX III program suite. Absorption corrections were performed using SADABS. Space groups were assigned by analysis of metric symmetry and systematic absences (determined by XPREP) and were further checked by PLATON 88,89 for additional symmetry. All of the structures were solved by direct methods and were refined against all data in the reported 2θ ranges by full-matrix least- squares on F2 with the SHELXL program suite using the OLEX 2 91interface. Hydrogen atoms at idealized positions were included during the final refinements of each structure. The OLEX 2 interface was used for structure visualization, analysis of bond distances, angles, and drawing ORTEP plots.

Homogeneous electrochemical experiments. Cyclic voltammograms were recorded on a potentiostat (CHI 700E or CHI720D) using glassy carbon as a working electrode. All CV data were collected in a sealed electrochemical cell. Five mL of 0.5 mM compound solution in ACN/THF(9:1) was taken in the presence of 100 mM TBAP as the supporting electrolyte. The glassy carbon electrode was taken as the working electrode, standard double-junction silver/silver chloride as the reference electrode, and a Pt was taken as the counter electrode. Ferrocene (Fc) was used as an internal reference, and the potential scale is normalized with respect to the potential of the $Fc^{+/0}$ couple. The solution was deaerated by bubbling N_2 or O_2 before recording the CV as required. All the electrochemical experiments were performed at room temperature

Heterogeneous electrochemical experiments: All electrochemical experiments were conducted in pH 7 buffer (unless otherwise mentioned) containing 100 mM $Na_2HPO_4.2H_2O$ and 100 mM KPF_6 (supporting electrolyte), using a Pt wire as the counter electrode and a double layer Ag/AgCl electrode as the

reference electrode. All electrochemical data were plotted following the polarographic convention. A 3-neck glass cell fitted with PTFE stoppers from Pine Research was used for all electrochemical experiments unless otherwise mentioned. Separation of the WE compartment from the CE compartment did not result in any difference in the data output. All experiments were conducted at 25 °C. Applied voltages were corrected for IR compensation by running the IR compensation test in the electrochemical workstation. For anaerobic experiments, the electrolyte was purged with

View Article Online
DOI: 10.1039/D6SC03084J

UHP-grade argon gas at a 10 mL/min flow rate. The starting point of the scan was fixed at 0.2 V, and the initial direction of the scan was cathodic. Electrochemical stability and purity of the catalyst at the electrode surface during electrochemical experiments were verified by taking CV for several cycles, where no visible changes were encountered in the $Fe^{III/II}$ potential and current density.

Attachment of Catalysts on SAM-Modified Ag and Au Electrodes. The SAM-modified Au and roughened Ag disks were taken out of the depositing solutions, rinsed with ethanol and a copious amount of water, and then mounted on the RRDE setup. The solutions of the catalysts were prepared in chloroform, followed by drop-casting onto the electrode for 30 minutes to ensure complete
loading. After each respective loading, the surfaces were thoroughly rinsed with chloroform, ethanol, and triply distilled water before carrying out electrochemical or SERRS/SERRS-RDE experiments.

UV-Vis Absorption Data Collection: Absorption spectra of the pure complexes were collected in ACN:THF (9:1) (2 mL; 5 μM). The background was corrected before the experiments, using an identical amount of solvent mixture.

^{1}H NMR Data Collection: ^{1}H NMR spectra were recorded on a 300 MHz NMR spectrometer. A 60 mM solution of the ligand was prepared in 400 μL of DMSO-d_6 containing a 10 mM internal standard, followed by the addition of H_2O**.** Two scans were collected to obtain spectra with clarity and the change in chemical shift value of the 2H's of H_2O was monitored after each addition.

Fluorescence Data Collection: The samples were excited with the respective excitation wavelength as obtained from absorption data. The emission spectra of the pure complexes were collected in ACN:THF (9:1) (2 mL; 5 μM).

TCSPC Data Collection: The life time experiments of the pure complexes were collected in ACN:THF (9:1) (2 mL; 5 μM). The decay traces are fitted using EzTime software and the quality of the fitting was judged by weighted residuals (close to 1). All the traces were described by single exponential function. The quality of fitting was evaluated from the weighted residual distribution

View Article Online
DOI: 10.1039/D6SC03084J

and the autocorrelation function of the weighted residuals. A satisfactory fit was confirmed when the weighted residuals were randomly distributed around zero, the autocorrelation function became close to the zero line, and the reduced chi-square value was close to unity.

Synthetic Details:

H_2MAPP (1)

MAPP was synthesized following the reported protocol from Collman and co-workers. ESI-MS(positive-ion mode, CH_2Cl_2): 630.2630 (100%, $[M + H]^+$) **(Figure S1)** , ^{1}H NMR ($CDCl_3$): δ (ppm) −2.66 (bs, 2H), 3.36 (s, 2H), 6.8–8.3 (m, 19 H), 8.6–9.1 (m, 8 H) **(Figure S2).**

H_2-biguanide (2)

MAPP **(1)** (1 eq, 400 mg, 0.634 mmol) was dissolved in 40 mL of dry THF. To this solution, dicyandiamide (1.5 eq, 80 mg, 0.952 mmol) and $AlCl_3$ (2 eq, 170 mg, 1.268 mmol) were added under reflux condition while maintaining an inert atmosphere. After 1 day 4eq of dicyanodiamide and 3eq of $AlCl_3$ was added extra and kept in refluxing condition for another 2 days. The organic layer in DCM was washed with saturated NH_4Cl and NaCl solution, collected and dried over anhydrous Na_2SO_4. The solvent was evaporated under reduced pressure and was purified through column chromatography using neutral alumina and 30% methanol-DCM solvent mixture. Hexagoanal purple crystal was obtained by slow vapour diffusion of the ether in DCM **(Fig.1b)**. Yield (410mg, 90.5%). ^{1}H NMR (300 MHz, DMSO-d_6) δ 8.99 (d, J = 4.8 Hz, 2H), 8.89 – 8.74 (m, 6H), 8.34 – 8.19 (m, 6H), 7.96 (dd, J = 7.5, 1.5 Hz, 1H), 7.82 (dq, J = 9.5, 5.3 Hz, 9H), 7.76 – 7.65 (m, 1H), 7.42 (d, J = 8.1 Hz, 1H), 7.31 (t, J = 7.4 Hz, 1H), 5.10 (s, 2H), -2.80 (s, 2H) **(Figure S3)**. ^{13}C NMR (101 MHz, DMSO-d_6) {^{1}H} δ 158.55, 156.87, 141.91, 141.85, 137.13, 135.43, 135.10, 134.75, 134.63, 130.80, 129.98, 128.92, 128.47, 128.24, 127.44, 127.17, 122.95, 120.04, 119.99. **(Figure S4).** ESI-MS (Positive ion mode, CH_2Cl_2): 714 ([M]+) **(Figure S5).** UV-Vis (THF λ/nm = 414, 512, 546, 587, 647) **(Figure S6).**

Fe-biguanide (3)

H_2-biguanide (2) (200 mg, 0.280 mmol, 1 eq) was dissolved in 20 mL of dry, degassed tetrahydrofuran (THF). To this solution, 2,4,6-collidine (74 µL, 0.560 mmol, 2 eq) was added to

View Article Online
DOI: 10.1039/D6SC03084J

deprotonate the pyrrolic protons, followed by the addition of $FeBr_2$ (240 mg, 1.12 mmol, 4 eq). The resulting mixture was stirred under an inert atmosphere for 48 hours. After completion, the reaction was quenched with water. The organic layer in DCM was washed with brine solution and 4N HCl, collected and dried over anhydrous Na_2SO_4 . The solvent was evaporated under reduced pressure. The product was purified through column chromatography using neutral alumina and 40% methanol-DCM solvent mixture. Yield (235mg, 91%). Anal. Calcd for C_{46} H_{34} Cl Fe N_9. $2CH_3OH$. CH_2Cl_2 : C= 61.81%, H= 4.55%, Cl= 11.17%, Fe= 5.87%, N=13.24%, O= 3.36%. Found: C= 60.62%, H=4.88%, Cl= 11.58%, Fe= 5.67%, N= 13.75%, O= 3.24%. ESI-MS (Positive ion mode, CH_2Cl): 768($[M]^+$) **(Figure S7).** UV-Vis (THF λ/nm = 415, 510, 583, 645, 690) **(Figure S6)**.

Zn-Biguanide (4)

H_2-biguanide (2) (1eq, 100mg, 0.140mmol) was dissolved in 15mL of dry THF. To this solution $Zn(OAc)_2$ (4eq, 123mg, 0.560mg) was added and stirred for 2hrs. No external base was added as the counter anion of Zn(II) salt used i.e acetate can deprotonate the pyrrolic protons. The organic layer in DCM was washed with a brine solution, collected and dried over anhydrous Na_2SO_4. The solvent was evaporated under reduced pressure. The product was purified through column chromatography using neutral alumina and 30% methanol-DCM solvent mixture. Yield (115mg, 90%). ESI-MS (Positive ion mode, CH_2Cl_2): 776 $([M+H])^+$ **(Figure S8)**.

H_2- triazine (5)

H_2-biguanide (2) (1eq, 100mg, 0.140mmol) was dissolved in 5mL methanol and 20mL ethylacetate to it NaOMe (10eq, 76mg, 1.40mmol) dissolved in methanol was added and kept in refluxing condition for 2 days. The organic layer in DCM was washed with NH_4Cl and NaCl collected and dried over anhydrous Na_2SO_4. The solvent was evaporated under reduced pressure and was purified through column chromatography using mesh size of 100-200 silica gel and 3% methanol-DCM solvent mixture. Yield (120mg, 89%).ESI-MS (Positive ion mode, CH_2Cl_2): 738 ($[M]^+$) **(Figure S9).** UV-Vis (THF λ/nm = 414, 511, 546, 587, 647) **(Figure S6).**

Fe-triazine (6)

H_2- triazine (5) (100 mg, 0.136 mmol, 1 eq) was dissolved in 20 mL of dry, degassed tetrahydrofuran (THF). To this solution, 2,4,6-collidine (36 µL, 0.271mmol, 2 eq) was added to deprotonate the pyrrolic protons, followed by the addition of $FeBr_2$ (160mg, 0.544 mmol, 4 eq). The

View Article Online
DOI: 10.1039/D6SC03084J

resulting mixture was stirred under an inert atmosphere for 48 hours. After completion, the reaction was quenched with water. The organic layer in DCM was washed with brine solution and 4N HCl, collected and dried over anhydrous Na_2SO_4 . The solvent was evaporated under reduced pressure. The product was purified through column chromatography using mesh size 100-200 silica gel and 10% methanol-DCM solvent mixture. Yield (110mg, 87.3%). Anal. Calcd for C_{48} H_{35} Cl Fe N_9. CH_3OH. $2CH_2Cl_2$: C= 59.41%, H= 4.20%, Cl= 17.19%, Fe= 5.42%, N=12.23%, O= 1.55%. Found: C= 60.01%, H=4.35%, Cl= 16.86%, Fe= 5.51%, N= 12.74%, O= 1.74%. ESI-MS (Positive ion mode, CH_2Cl_2): 791([M]+) **(Figure S10)**. UV-Vis (THF λ/nm = 415, 510, 583, 647, 691) **(Figure S6)**.

Zn-triazine (7)

H_2-biguanide (2) (1eq, 50mg, 0.063mmol) was dissolved in 15mL of dry THF. To this solution Zn(OAc)2 (4eq, 55mg, 0.252mg) was added and stirred for 2hrs. No external base was added as the counter anion of Zn(II) salt used i.e acetate can deprotonate the pyrrolic protons. The organic layer in DCM was washed with a brine solution, collected and dried over anhydrous Na_2SO_4. The solvent was evaporated under reduced pressure. The product was purified through column chromatography using mesh size 100-200 silica gel and 5% methanol-DCM solvent mixture. Yield (55mg, 88.14%). ESI-MS (Positive ion mode, CH_2Cl_2): 800 $([M+H])^+$ **(Figure S11)**.

Associated Content

Supporting Information

The Supporting Information is available free of charge at ( ) . Additional UV−vis, HRMS, ^{1}H-NMR, electrochemistry data and rR data.

Accession Codes

CCDC 2540588 contain the supporting crystallographic data for this paper. These data can be obtained free of charge via www.ccdc.cam.ac.uk/data_request/cif, by emailing at data_request@ccdc.cam.ac.uk, or by contacting the Cambridge Crystallographic Data Centre, 12 Union Road, Cambridge CB2 1EZ, U.K.; fax: + 441223 336033.

Author information

Corresponding Author

View Article Online
DOI: 10.1039/D6SC03084J

Abhishek Dey – School of Chemical Sciences, Indian Association for the Cultivation of Science, Kolkata, West Bengal 700032, India; orcid.org/0000-0002-9166-3349; Email: abbeyde@gmail.com

Authors

Suman Patra – School of Chemical Sciences, Indian Association for the Cultivation of Science, Kolkata, West Bengal 700032, India

Soumili Ghosh – School of Chemical Sciences, Indian Association for the Cultivation of Science, Kolkata, West Bengal 700032, India

Soumya Samanta – School of Chemical Sciences, Indian Association for the Cultivation of Science, Kolkata, West Bengal 700032, India

Nisha Maurya – School of Chemical Sciences, Indian Association for the Cultivation of Science, Kolkata, West Bengal 700032, India

Somnath Das– School of Chemical Sciences, Indian Association for the Cultivation of Science, Kolkata, West Bengal 700032, India

Complete contact information is available at:

Author Contributions

† Suman Patra and Soumili Ghosh contributed equally to this work.

Conflicts of interest

The authors declare no competing financial interest.

Acknowledgments

This research was funded by the Department of Science and Technology, JC Bose grant (ANRF/JBG/2025/000017/CS). S.P. and S.G. acknowledge CSIR-India for the Senior Research Fellowship (SRF). S.S. acknowledges CSIR SPM-SRF fellowship. N.M. and S.D. acknowledges IACS Institute-JRF and SRF respectively.

References:

1 Z. Liang, H. Lei, H. Zheng, H.-Y. Wang, W. Zhang and R. Cao, *Chem. Soc. Rev.*, 2025, **54**, 5248–5291.

View Article Online
DOI: 10.1039/D6SC03084J

2 S. Chatterjee, K. Sengupta, B. Mondal, S. Dey and A. Dey, *Acc. Chem. Res.*, 2017, **50**, 1744–1753.

3 M. L. Pegis, C. F. Wise, D. J. Martin and J. M. Mayer, *Chem. Rev.*, 2018, **118**, 2340–2391.

4 W. Nam, *Acc. Chem. Res.*, 2015, **48**, 2415–2423.

5 M. Shao, Q. Chang, J.-P. Dodelet and R. Chenitz, *Chem. Rev.*, 2016, **116**, 3594–3657.

6 M. Liu, Y. Zhao, Q. Chang, H. Zhou, M. Gennari, C. Duboc and L. Wang, *Inorg. Chem. Front.*, DOI:10.1039/D5QI02259B.

7 S. Bhunia, A. Ghatak and A. Dey, *Chem. Rev.*, 2022, **122**, 12370–12426.

8 S. Dey, B. Mondal, S. Chatterjee, A. Rana, S. Amanullah and A. Dey, *Nat. Rev. Chem.*, 2017, **1**, 98.

9 S. Sinha, M. Ghosh and J. J. Warren, *ACS Catal.*, 2019, **9**, 2685–2691.

10 W. D. Bailey, D. Dhar, A. C. Cramblitt and W. B. Tolman, *J. Am. Chem. Soc.*, 2019, **141**, 5470–5480.

11 M. L. Pegis, D. J. Martin, C. F. Wise, A. C. Brezny, S. I. Johnson, L. E. Johnson, N. Kumar, S. Raugei and J. M. Mayer, *J. Am. Chem. Soc.*, 2019, **141**, 8315–8326.

12 A. Santra, A. Das, S. Kaur, P. Jain, P. P. Ingole and S. Paria, *Chem. Sci.*, 2024, **15**, 4095–4105.

13 A. Singha, A. Mondal, A. Nayek, S. G. Dey and A. Dey, *J. Am. Chem. Soc.*, 2020, **142**, 21810–21828.

14 A. Singha and A. Dey, *Chem. Commun.*, 2019, **55**, 5591–5594.

15 R. Oliveira, W. Zouari, C. Herrero, F. Banse, B. Schöllhorn, C. Fave and E. Anxolabéhère-Mallart, *Inorg. Chem.*, 2016, **55**, 12204–12210.

16 D. Ricard, M. L'Her, P. Richard and B. Boitrel, *Chem. – A Eur. J.*, 2001, **7**, 3291–3297.

17 X. Zhang, J. Zhan, H. Qin, J. Deng, J. Liu, M. Li, R. Cao and Y. Shao, *Chem. Sci.*, 2025, **16**, 5512–5517.

18 S. L. George, L. Zhao, Z. Wang, Z. Xue and L. Zhao, 2024, DOI: 10.3390/molecules29235655.

19 L. Xie, X.-P. Zhang, B. Zhao, P. Li, J. Qi, X. Guo, B. Wang, H. Lei, W. Zhang, U.-P. Apfel and R. Cao, *Angew. Chemie Int. Ed.*, 2021, **60**, 7576–7581.

20 S. Dinda, T. Roy, S. Sengupta, P. Baidya and A. Dey, *JACS Au*, 2025, **5**, 6275–6286.

21 A. Ghatak, S. Bhunia and A. Dey, *ACS Catal.*, 2020, **10**, 13136–13148.

22 A. Ghatak, S. Bhakta, S. Bhunia and A. Dey, *Chem. Sci.*, 2019, **10**, 9692–9698.

23 S. Chatterjee, K. Sengupta, S. Samanta, P. K. Das and A. Dey, *Inorg. Chem.*, 2013, **52**, 9897–9907.

View Article Online
DOI: 10.1039/D6SC03084J

24 K. Sengupta, S. Chatterjee, S. Samanta, S. Bandyopadhyay and A. Dey, *Inorg. Chem.*, 2013, **52**, 2000–2014.

25 S. Chattopadhyay, S. Samanta, A. Sarkar, A. Bhattacharya, S. Patra and A. Dey, *J. Chem. Phys.*, 2023, **158**, 44201.

26 K. Mittra, S. Chatterjee, S. Samanta and A. Dey, *Inorg. Chem.*, 2013, **52**, 14317–14325.

27 S. Chatterjee, K. Sengupta, S. Samanta, P. K. Das and A. Dey, *Inorg. Chem.*, 2015, **54**, 2383–2392.

28 H. Qin, Y. Wang, T. Liu, Y. Xu, H. Lei, X. Li, W. Zhang, S. Fukuzumi, W. Nam and R. Cao, *J. Am. Chem. Soc.*, 2026, **148**, 933–943.

29 S. Amanullah, P. Saha and A. Dey, *Faraday Discuss.*, 2022, **234**, 143–158.

30 M. L. Pegis, B. A. McKeown, N. Kumar, K. Lang, D. J. Wasylenko, X. P. Zhang, S. Raugei and J. M. Mayer, *ACS Cent. Sci.*, 2016, **2**, 850–856.

31 S. Chatterjee, K. Sengupta, S. Hematian, K. D. Karlin and A. Dey, *J. Am. Chem. Soc.*, 2015, **137**, 12897–12905.

32 A. C. Brezny, S. I. Johnson, S. Raugei and J. M. Mayer, *J. Am. Chem. Soc.*, 2020, **142**, 4108–4113.

33 X. Huang and J. T. Groves, *Chem. Rev.*, 2018, **118**, 2491–2553.

34 S. Bhunia, A. Rana, P. Roy, D. J. Martin, M. L. Pegis, B. Roy and A. Dey, *J. Am. Chem. Soc.*, 2018, **140**, 9444–9457.

35 S. Bhunia, A. Ghatak, A. Rana and A. Dey, *J. Am. Chem. Soc.*, 2023, **145**, 3812–3825.

36 C. T. Carver, B. D. Matson and J. M. Mayer, *J. Am. Chem. Soc.*, 2012, **134**, 5444–5447.

37 A. Ghatak, S. Samanta, A. Nayek, S. Mukherjee, S. G. Dey and A. Dey, *Inorg. Chem.*, 2022, **61**, 12931–12947.

38 S. Mukherjee, A. Nayek, S. Bhunia, S. G. Dey and A. Dey, *Inorg. Chem.*, 2020, **59**, 14564–14576.

39 S. Ghosh, S. Patra, A. Bisoi, S. Ghosh, N. Maurya, A. Das, P. C. Singh and A. Dey, *ACS Catal.*, 2025, **15**, 3595–3610.

40 J. Langmaier, M. Pižl, Z. Samec and S. Záliš, *J. Phys. Chem. A*, 2016, **120**, 7344–7350.

41 L. F. Javitt, I. Weissbuch, D. Ehre, I. Lubomirsky and M. Lahav, *Cryst. Growth Des.*, 2022, **22**, 43–47.

42 E. S. Stoyanov, I. V Stoyanova and C. A. Reed, *J. Am. Chem. Soc.*, 2010, **132**, 1484–1485.

43 O. Grytsai, C. Ronco and R. Benhida, *Beilstein J. Org. Chem.*, 2021, **17**, 1001–1040.

44 J. P. Collman, R. Boulatov, C. J. Sunderland and L. Fu, *Chem. Rev.*, 2004, **104**, 561–588.

45 S. Samanta, S. Sengupta, S. Biswas, S. Ghosh, S. Barman and A. Dey, *J. Am. Chem. Soc.*, 2023, **145**, 26477–26486.

46 K. L. Davis, B. J. Drews, H. Yue, D. H. Waldeck, K. Knorr and R. A. Clark, *J. Phys. Chem. C*, 2008, **112**, 6571–6576.

View Article Online
DOI: 10.1039/D6SC03084J

47 A. Hosseini, J. P. Collman, A. Devadoss, G. Y. Williams, C. J. Barile and T. A. Eberspacher, *Langmuir*, 2010, **26**, 17674–17678.

48 J. B. Shein, L. M. H. Lai, P. K. Eggers, M. N. Paddon-Row and J. J. Gooding, *Langmuir*, 2009, **25**, 11121–11128.

49 J. P. Collman, N. K. Devaraj, R. A. Decréau, Y. Yang, Y.-L. Yan, W. Ebina, T. A. Eberspacher and C. E. D. Chidsey, *Science (80-.).*, 2007, **315**, 1565–1568.

50 K. Sengupta, S. Chatterjee, S. Samanta and A. Dey, *Proc. Natl. Acad. Sci.*, 2013, **110**, 8431–8436.

51 K. Sengupta, S. Chatterjee and A. Dey, *ACS Catal.*, 2016, **6**, 6838–6852.

52 T. G. Spiro, *Acc. Chem. Res.*, 1974, **7**, 339–344.

53 T. G. Spiro and T. C. Strekas, *J. Am. Chem. Soc.*, 1974, **96**, 338–345.

54 J. M. Burke, J. R. Kincaid, S. Peters, R. R. Gagne, J. P. Collman and T. G. Spiro, *J. Am. Chem. Soc.*, 1978, **100**, 6083–6088.

55 K. Mittra, K. Sengupta, A. Singha, S. Bandyopadhyay, S. Chatterjee, A. Rana, S. Samanta and A. Dey, *J. Inorg. Biochem.*, 2016, **155**, 82–91.

56 T. Ogura, S. Takahashi, S. Hirota, K. Shinzawa-Itoh, S. Yoshikawa, E. H. Appelman and T. Kitagawa, *J. Am. Chem. Soc.*, 1993, **115**, 8527–8536.

57 W. Jiang, M. Zhou, K. Chen, X. Xiao, J. Shi, H. Zhang, J. Xie, S. Chen, M. Chen, Z. Cong, L. Liu, Y. Wu and R. Liu, *Nat. Commun.*, 2025, **17**, 336.

View Article Online
DOI: 10.1039/D6SC03084J

The experimental data presented in the manuscript will be made available upon reasonable request.